

Plasma Actuators for Cylinder Flow Control and Noise Reduction

Flint O. Thomas,* Alexey Kozlov,† and Thomas C. Corke‡
University of Notre Dame, Notre Dame, Indiana 46556

DOI: 10.2514/1.27821

In this paper, the results of flow-control experiments using single dielectric barrier discharge plasma actuators to control flow separation and unsteady vortex shedding from a circular cylinder in crossflow are reported. This work is motivated by the need to reduce landing gear noise for commercial transport aircraft via an effective streamlining created by the actuators. The experiments are performed at $Re_D = 3.3 \times 10^4$. Using either steady or unsteady actuation, Karman shedding is totally eliminated, turbulence levels in the wake decrease significantly, and near-field sound pressure levels associated with shedding are reduced by 13.3 dB. In the case of unsteady plasma actuation, an actuation frequency of $St_D = 1$ is found to be most effective. The unsteady actuation has the advantage that total suppression of shedding is achieved for a duty cycle of only 25%. However, because unsteady actuation is associated with an unsteady body force and produces a tone at the actuation frequency, steady actuation is more suitable for noise-control applications.

Nomenclature

C_μ	=	momentum coefficient
D	=	cylinder diameter
\mathbf{E}	=	electric field vector
f	=	temporal frequency
\mathbf{f}_b^*	=	body force (per unit volume) vector
Re_D	=	Reynolds number based on cylinder diameter
St_D	=	Strouhal number based on cylinder diameter
U_∞	=	freestream velocity
V_J	=	wall jet velocity
x	=	streamwise spatial coordinate
y	=	wall-normal spatial coordinate
ρ	=	fluid density
ρ_c	=	charge density

I. Introduction

PROJECTED increases in civil air traffic coupled with a larger population in the vicinity of major airports will result in continued pressure to reduce aircraft noise on takeoff and landing. The jet noise component of overall aircraft noise has been significantly reduced by the use of engines with high-bypass ratio. In landing approach, when engines are throttled down, the airframe now represents a primary noise source. This has spawned considerable interest in understanding the physical mechanisms responsible for airframe noise production and how they can be controlled. A combination of experimental and computational airframe noise research has identified key airframe noise sources that appear generic to the current generation of commercial transport aircraft. These include 1) landing gear noise associated with flow past landing gear

struts, uncovered wheel wells, and undercarriage elements, and 2) high-lift system noise associated with trailing flap side edge, leading edge slats, and the associated brackets and rigging. Although the detailed physical mechanisms of noise production from these sources may differ and are still a focus of active investigation, it is clear that a common feature of each is a region of unsteady, separated flow. Consequently, any flow-control strategy, either active or passive, that eliminates or minimizes such flow separations will likely have a significant effect on reducing the associated airframe noise. Hence, it is not surprising to find that separation control is at the core of many noise-control strategies currently under investigation for commercial transport aircraft.

Flyover tests have shown that landing gear noise represents a primary source of airframe noise (Michel et al. [1]). As noted by Lazos [2], the inherent bluff-body characteristics of landing gear give rise to large-scale flow separation that results in noise production through unsteady wake flow and large-scale vortex instability and deformation. Large-scale, unsteady, Reynolds-averaged Navier–Stokes simulations of the flowfield over a landing gear assembly have been performed by Li et al. [3]. These simulations capture the unsteady vortex shedding that occurs from the oleo and struts as well as the flow from the landing gear wheels. This study also serves to demonstrate the extreme complexity of the unsteady separated flow over the gear. A full aeroacoustic analysis of a landing gear assembly was recently reported by Lockard et al. [4]. Data from an unsteady Reynolds-averaged Navier–Stokes simulation of the flow over a landing gear assembly was used as input to the Ffowcs Williams–Hawking equation (Ffowcs Williams and Hawkings [5]) to predict the noise at far-field observer locations.

Major components of the landing gear take the form of bluff bodies in crossflow. Passive flow control in the form of fairings designed to reduce flow separation over landing gear elements has been studied experimentally. These investigations show that a faired landing gear generates considerably less noise than the corresponding unmodified gear. However, its use is limited by practical considerations like the need to allow easy access for gear maintenance and the ability to stow the gear in cruise. Certainly, their added weight is also a consideration. Similarly, active blowing or suction strategies must deal with the increased part count and maintenance costs associated with complex bleed air-ducting systems.

We have been involved in the development and use of single dielectric barrier discharge (SDBD) plasma actuators in several applications of active aerodynamic separation control. These studies have demonstrated that plasma actuators are ideally suited to flow separation control in a wide variety of aerodynamic applications.

Presented as Paper 2845 at the 3rd AIAA Flow Control Conference, San Francisco, CA, 5–8 June 2006; received 14 September 2006; revision received 12 December 2007; accepted for publication 26 December 2007. Copyright © 2008 by the American Institute of Aeronautics and Astronautics, Inc. All rights reserved. Copies of this paper may be made for personal or internal use, on condition that the copier pay the \$10.00 per-copy fee to the Copyright Clearance Center, Inc., 222 Rosewood Drive, Danvers, MA 01923; include the code 0001-1452/08 \$10.00 in correspondence with the CCC.

*Professor, Department of Aerospace and Mechanical Engineering, Center for Flow Physics and Control. Associate Fellow AIAA.

†Graduate Research Assistant, Department of Aerospace and Mechanical Engineering, Center for Flow Physics and Control.

‡Clark Equipment Professor, Department of Aerospace and Mechanical Engineering, Center for Flow Physics and Control. Associate Fellow AIAA.

Because, as described previously, landing gear noise originates from unsteady, separated flow from bluff-body gear elements, the use of plasma actuators to actively reduce gear noise appears promising.

II. Objective

Motivated by potential landing gear noise-control applications, a primary objective of this paper is to demonstrate the use of surface-mounted SDBD plasma actuators to create a “plasma fairing” that effectively streamlines a circular cylinder in crossflow by active means. For these proof-of-concept flow-control experiments, the cylinder in crossflow is chosen for study because it represents a generic flow geometry that is similar in all essential aspects to a landing gear oleo or strut. By minimizing the unsteady flow separation from the cylinder and associated large-scale wake vorticity, the radiated aerodynamic noise is also influenced. In the next section, a brief overview of the basic principle of operation of the SDBD plasma actuators is presented. This is followed by a description of the cylinder flow-control experiment and wind-tunnel facility.

III. Single Dielectric Barrier Discharge Plasma Actuators

A single dielectric barrier discharge forms the basis for the plasma actuators used in this investigation (e.g., Fridman and Kennedy [6]). This type of plasma discharge has the unique property that it can sustain a large volume discharge at atmospheric pressure *without arcing* because it is self-limiting. The basic characteristics of SDBD plasma actuators are described in Enloe et al. [7,8].

As shown in Fig. 1, a plasma actuator consists of two electrodes that are separated by a dielectric barrier material. The two electrodes are given a slight overlap. When a sufficiently high ac voltage input is supplied to the electrodes, the dielectric barrier discharge ignites. The physical structure of SDBD is described in Gibalov and Pietsch [9]. The charge multiplication and air ionization mechanism is similar to the corona discharge process described in Raizer [10]. Ionization generally starts at the edge of the electrode that is exposed to the air, where the intensity of the electric field has its largest value. When the magnitude of this electric field is high enough, electron avalanches followed by streamer formation are produced. Streamers are thin ionized channels between the electrodes with a lifetime of the order of 10 ns. They begin at the exposed electrode edge and terminate at the dielectric surface. Because of their relatively high conductivity, the streamers efficiently transfer electric charge from the exposed electrode to the plasma volume near the dielectric surface. Because this volume charge has the same sign as the exposed electrode, the electrostatic force repels it from the exposed electrode and attracts it to the dielectric surface above the covered electrode. This buildup of surface charge on the dielectric opposes the applied voltage and gives the plasma discharge its self-limiting character. That is, the plasma is extinguished unless the magnitude of the applied voltage continuously increases. The charge transfer process repeats in the opposite direction during the second half of the ac cycle (i.e., from dielectric surface back to the exposed electrode). The formation of the plasma gives rise to a body force on the ambient air. It is the resulting coupling of directed momentum to the surrounding air that forms the basis for flow-control strategies. Although the direction of

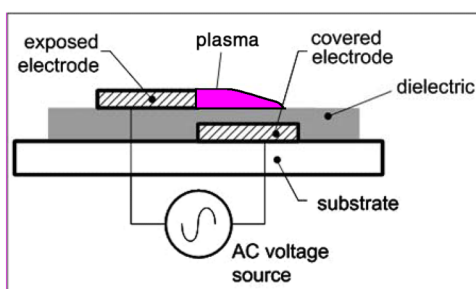


Fig. 1 Schematic of the SDBD plasma actuator.

charge transfer varies during the two halves of the ac cycle, the body force always has the same direction. The body force vector is given by

$$\mathbf{f}_b^* = \rho_c \mathbf{E}$$

Of importance is the fact that the body force and induced velocity can be tailored through the design of the electrode arrangement, which controls the spatial electric field. For example, Post [11] has demonstrated electrode arrangements that could produce wall jets, spanwise vortices, or streamwise vortices when placed on the wall in a boundary layer. For the electrode geometry shown in Fig. 1, air is accelerated along the dielectric surface from the edge of exposed electrode toward the far end of the covered electrode, thereby giving rise to a wall jet effect. It will be shown that an array of this type of SDBD plasma actuators mounted on the surface of a cylinder gives rise to a plasma-fairing effect in which the cylinder in crossflow is effectively streamlined.

IV. Flow-Control Experiments

A. Experimental Apparatus and Flowfield Facility

To experimentally demonstrate the plasma-fairing concept, consideration is given to the application of four surface-mounted SDBD plasma actuators to control unsteady separation from a circular cylinder in crossflow. This section describes the cylinder model and wind-tunnel facilities used for the experiments.

1. Wind-Tunnel Facility

The flow-control experiments were performed in one of the low-turbulence, subsonic, in-draft wind tunnels located at the Hessert Laboratory for Aerospace Research at the University of Notre Dame. The wind tunnel has an inlet with contraction ratio of 20:1. A series of 12 turbulence management screens at the front of the inlet give rise to tunnel freestream turbulence levels less than 0.1% (and less than 0.06% for frequencies above 10 Hz). Experiments are performed in a test section of 0.610 m square cross section and 1.82 m in length. One sidewall has optical access for nonintrusive laser flowfield diagnostics (particle image velocimetry [PIV]).

2. Application of Single Dielectric Barrier Discharge Plasma Actuators to a Cylinder Model

Figure 2 presents a schematic of four dielectric barrier discharge plasma actuators mounted on a circular cylinder model. The cylinder model takes the form of a quartz glass cylinder (1) with an outer diameter $D = 100$ mm, wall thickness $d = 2.5$ mm, and dielectric constant of 3.7. The cylinder diameter was driven by a “packing constraint” imposed by the need to mount four actuators on the cylinder. This constraint arises from a need to have a sufficient length of covered electrode so that full plasma formation can occur and by the recognition that multiple actuators must be placed sufficiently far apart so that plasma does not form on the upstream edge of a downstream exposed electrode. In the experiments reported here, this gave rise to a cylinder diameter that produced a blockage ratio of 16.7%. Drag coefficient measurements were performed using a pitot

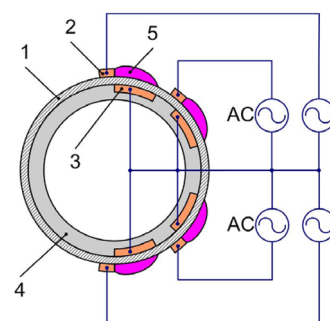


Fig. 2 Schematic of four SDBD plasma actuators mounted on the cylinder model.

probe traverse in conjunction with an integral momentum balance [12]. After applying appropriate blockage corrections, the expected drag coefficient for the unactuated cylinder in crossflow was obtained. Hence, the essential character of the cylinder flow is not altered by the blockage effect. Further, in this study it is the relative character of the actuated versus nonactuated flow that is of most interest, and this will not be significantly influenced by this degree of blockage.

In the configuration shown in Fig. 2, the cylinder wall serves as the dielectric barrier for the SDBD plasma. The ends of the cylinder terminate in Plexiglas endplates that prevent cylinder flow interaction with the tunnel sidewall boundary layers. As indicated, the outer, exposed electrodes (2) are mounted to the surface of the cylinder with their plasma-generating edges located at ± 90 and ± 135 deg with respect to the approach flow direction. These surface electrodes are made of 1.6 mil thick copper foil tape of width 5.6 mm. This choice for the electrode positioning results from the idea that the best location for the first pair of plasma actuators is near the separation point [13,14]. The second pair of actuators is placed downstream in an attempt to provide sufficient body force to prolong flow attachment on the back side of the cylinder via a plasma-induced Coanda effect. Note that the thickness of the electrodes is greatly exaggerated in Fig. 2. The corresponding four inner electrodes (3) are mounted to the inner surface of the cylinder. They are each made of 1.6 mil thick lead foil tape of 25.4 mm width. Both inner and outer electrodes extend 0.508 m in the spanwise direction. Seven layers of 5-mil-thick Kapton tape (4) cover the inner electrodes and serve to prevent inner discharge. Each inner and outer electrode pair has a small overlap, which gives rise to a large local electric field gradient. Plasma (5) forms near the edge of the exposed electrode and extends a distance along the cylinder's dielectric surface as depicted in Fig. 2. As indicated in the figure, the actuators are each connected to a high-voltage ac source that provides 8.1 kV rms sinusoidal excitation (≈ 11.5 kV amplitude) to the electrodes at a frequency of 10 kHz. This frequency is considerably higher than any relevant time scales associated with the flow. Hence the resulting body force on the ambient fluid may be considered effectively constant, and the resulting actuation is termed "steady." The case of unsteady actuation will be discussed later in the paper. The mean power dissipation was measured directly by using a high-voltage probe in conjunction with a current meter. In steady mode, the power dissipation was approximately 100 W for each actuator (power dissipation per unit length in the spanwise direction was approximately 200 W/m). It is correspondingly less for unsteady actuation due to a lower duty cycle as described in Sec. III.

The high-frequency, high-amplitude ac voltage is created using the circuit shown in Fig. 3. A low-amplitude waveform (in this case a sinusoidal signal) from a function generator (Stanford Research Systems DS335) is first supplied to twin, two-channel power amplifier units (Crown CE4000) forming four power amplification channels. The amplified voltage from each channel is then fed through a 1.2 Ω , 300 W resistor into the primary coil of a 1:180 transformer (Corona Magnetics) to increase the voltage level to

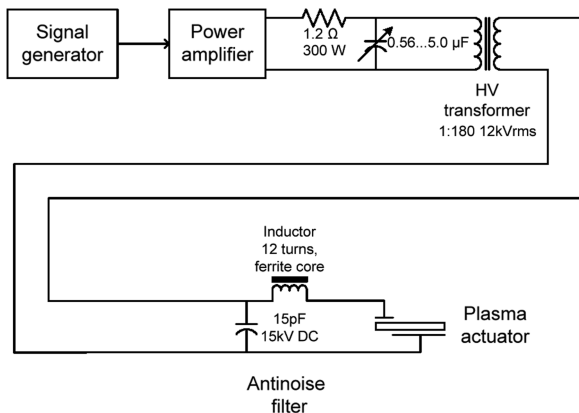


Fig. 3 Plasma-actuator circuit schematic (one channel shown).

8.1 kV rms. The resistor limits the current through the primary coil. A switched capacitor set is connected in parallel to the primary coil of the transformer to adjust the resonant frequency of the system. The high voltage for the excitation of the plasma actuators is obtained from the secondary coil of the transformer. Each of the four channels is used to feed one plasma actuator.

Dielectric barrier discharge is accompanied by high-intensity radio frequency electromagnetic noise. An antinoise filter was designed to suppress this noise. The custom-made filter is installed inside the cylinder model. In essence, it is a low-pass filter consisting of an inductor (12 turns, ferrite core, 31.1 mm OD, 19.1 mm ID, 15.9 mm H) and high-voltage capacitor (15 pF, 15 kV DC max). The filter does not affect the 10 kHz actuating frequency but prevents high-frequency noise from entering the high-voltage wires that feed the plasma actuators.

3. Steady and Unsteady Actuation

The single dielectric barrier discharge requires an ac voltage for its sustenance. However, if the time scale associated with the ac signal driving plasma formation is sufficiently small in relation to any relevant time scales for the flow, the associated body force produced by the plasma may be considered effectively steady. Certainly this is the case for the 10 kHz excitation used for the plasma generation on the cylinder model. However, unsteady actuation may also be applied, and signals for steady versus unsteady actuation are contrasted in Fig. 4. Note that both use the same high-frequency sinusoid. As shown in the figure, for unsteady actuation, it is apparent that during time interval T_1 , the plasma actuator is on only during the subinterval T_2 . Hence, the signal sent to the actuator has a characteristic frequency of $f = 1/T_1$ that will be much lower than that of the sinusoid and comparable to some relevant frequency of the flow. In addition, an associated duty cycle T_2/T_1 may be defined. Obviously, the unsteady actuation frequency and duty cycle may be independently controlled for a given flow-control application.

Two types of the unsteady actuation are used for the cylinder flow-control experiments reported in this paper. Symmetric unsteady actuation involved firing all four actuators simultaneously. Asymmetric actuation involved firing the top and bottom pair of actuators in antiphase.

4. Actuator-Induced Velocity Field

Before characterizing the behavior of the "plasma-faired" cylinder in the wind tunnel, the flow induced solely by a single surface-mounted plasma actuator was examined. Figure 5 presents the plasma-induced flow near the cylinder surface (in the absence of

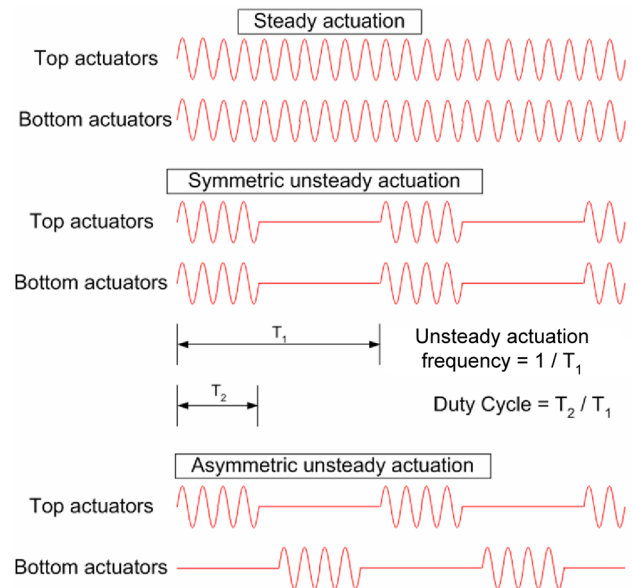


Fig. 4 Steady and unsteady actuation signals.

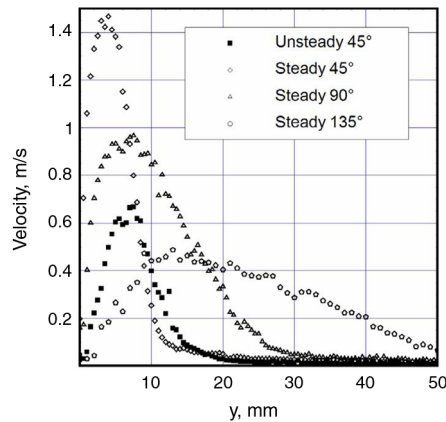


Fig. 5 Mean velocity profiles on the cylinder induced by a single surface-mounted actuator without external flow.

external flow) resulting from the operation of a single actuator. This is presented in the form of wall-normal mean velocity profiles for azimuthal locations 45, 90, and 135 deg relative to the actuator location. Constant temperature hot-wire anemometry was used to measure the mean velocity, which has an absolute uncertainty of ± 0.04 m/s. This figure shows that the body force associated with the SDBD actuator effectively produces local tangential blowing that adheres to the surface of the cylinder via an apparent Coanda effect. For steady, plasma-induced blowing, a wall jet forms, and flow separation from the cylinder occurs near 180 deg. The mean velocity profile corresponding to unsteady actuation is also shown for comparison at the 45 deg location and is observed to be thicker than the corresponding steady profile. This is due to the formation of discrete vortices that leave the surface in the unsteady actuation case. Strictly speaking, the momentum coefficient C_{μ} for the plasma actuation is zero because there is no momentum injection at the wall. However, if C_{μ} is calculated based on the integrated momentum flux,

$$C_{\mu} \equiv \frac{\int_0^{\infty} \rho V_j^2(y) dy}{1/2 \rho U_{\infty}^2 D}$$

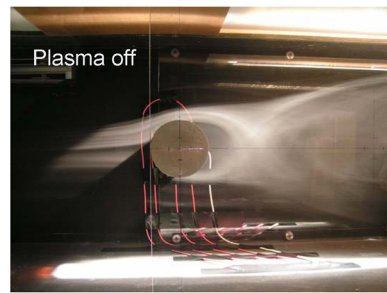
across the profiles shown in Fig. 5 for the 45 deg location, values of 1.1 and 0.3% are obtained for the steady and unsteady cases, respectively.

B. Experimental Results

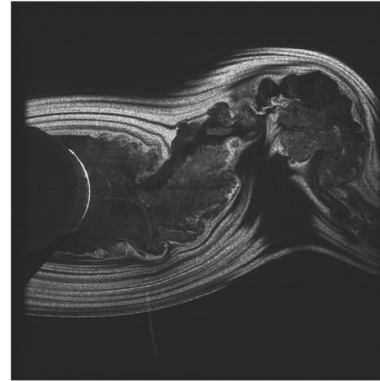
This section summarizes a series of flow-control experiments using four SDBD plasma actuators flush mounted on a circular cylinder in crossflow as described previously in Sec. IV.A. This work extends initial experiments using twin actuators placed at the top and bottom of a cylinder that were reported previously by Thomas et al. [12]. Unless otherwise noted, the Reynolds number for the current series of experiments (based on free stream velocity $U_{\infty} = 4 \pm 0.1$ m/s and cylinder diameter) is approximately $Re_D = 3.3 \times 10^4$. Measurements to be presented include flow visualization, wake mean velocity and turbulence intensity profiles, velocity autospectra, phase-locked particle image velocimetry of the near wake, and microphone sound pressure level measurements to characterize the near-field pressure fluctuations. All of these were performed both with and without plasma actuation.

1. Flow Visualization Results

The influence of the plasma actuators on the global structure of the cylinder flow is presented first. The flow with the actuators off is shown in Fig. 6a. Here the flow visualization was accomplished by introducing continuous smoke streaklines upstream of the wind-tunnel inlet contraction. The smoke generator is described by Mueller [15] and used propylene glycol as the smoke-producing fluid. The smoke streaklines were contained in the spanwise centerplane of the wind-tunnel test section, where they were illuminated by a high-intensity photo floodlight. Figure 6b shows a



a)



b)

Fig. 6 a) Smoke-flow visualization image with the plasma actuators off. b) Near-wake PIV flow visualization image with the plasma actuators off.

corresponding PIV image of the cylinder near wake obtained by seeding the flow with 1- μ m-diam olive oil droplets. These are illuminated by a pulsed Nd-Yag laser. With the actuators off, the flow obviously undergoes subcritical separation leading to a large-scale separated flow region that is accompanied by unsteady, Karman vortex shedding at a Strouhal number of 0.21 (approximately 9 Hz in the present experiment). Along with Karman vortex shedding, Fig. 6b clearly shows the presence of smaller scale Bloor-Gerrard vortices (as investigated by Bloor [16] and Gerrard [17]) that result from the convective instability of the separated shear layer. These occur at a frequency of approximately 150 Hz, which is consistent with data summarized in Williamson [18].

Figures 7a and 7b present corresponding flow visualization images with the four plasma actuators operating in steady mode. These figures show that the plasma actuation has a profound influence on the global structure of the flow. The plasma actuators are shown to substantially reduce the extent of the separated flow region, and the associated Karman vortex shedding appears to be eliminated. With the actuators on, the flow streaklines possess strong top-bottom, as well as fore-aft, symmetry indicating that the flow separation from the cylinder has been greatly reduced. That the flow remains attached over a much larger extent of the cylinder surface is likely associated with the Coanda effect demonstrated previously in Fig. 5, which serves to channel comparatively high-momentum fluid to the near-wall region with a consequent favorable effect on maintaining flow attachment. Flow visualization was also used to initially characterize the effect of unsteady plasma actuation. The duty cycle was fixed at 25%, and the unsteady actuation frequency was varied over a wide range. In each case, the plasma actuators were fired either symmetrically or asymmetrically. Symmetric plasma excitation at frequencies near the natural shedding frequency of $St_D = 0.21$ were found to give rise to large-amplitude, unsteady Karman vortex shedding at the subharmonic of the unsteady actuation frequency. Because a primary goal of the investigation was the suppression of shedding, the use of higher-frequency excitation was explored. It was found that optimum suppression of shedding and minimum wake defect occurred for unsteady forcing at a frequency of approximately 50 Hz, which is over five times the cylinder-shedding frequency. Figures 8 and 9 show sample flow

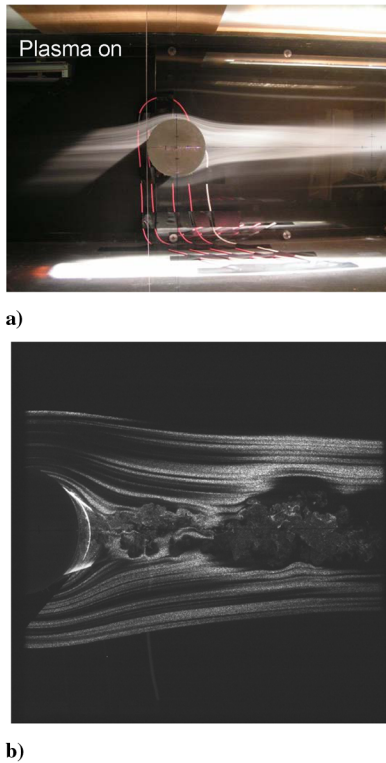


Fig. 7 a) Smoke-flow visualization image with the plasma actuators on (steady actuation). b) Near-wake PIV flow visualization image with the plasma actuators on (steady actuation).

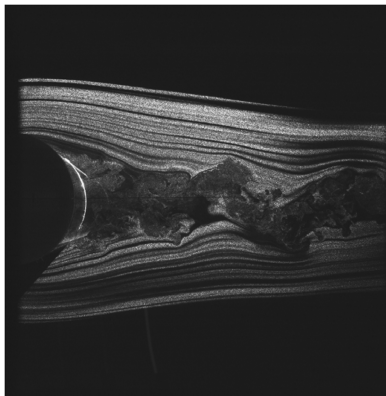


Fig. 8 Unsteady symmetric plasma actuation at excitation $St_D = 1$ and 25% duty cycle ($Re_D = 3.3 \times 10^4$).

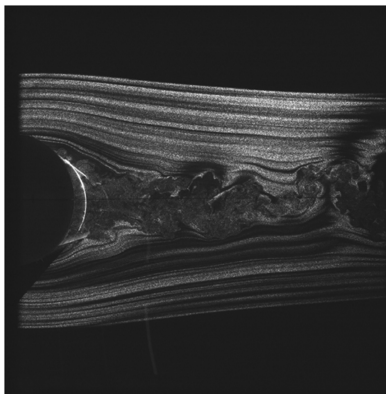


Fig. 9 Unsteady asymmetric plasma actuation at excitation $St_D = 1$, and 25% duty cycle ($Re_D = 3.3 \times 10^4$).

visualization images obtained with unsteady symmetric and asymmetric 50 Hz excitation at 25% duty cycle. In both of these images, the near wake has been considerably reduced in width from that shown in Fig. 6, Karman vortex shedding is again eliminated, and the cylinder appears to have been effectively streamlined by the plasma actuators.

It is important to point out that the optimum actuation frequency of 50 Hz corresponds to a Strouhal number (based on freestream velocity and cylinder diameter) of $St_D = fD/U_\infty = 1$. This is perhaps not surprising because the excitation Strouhal number may be thought of as a ratio between the time scale for actuation $1/f$, and the characteristic time scale for the separated flow region ($\mathcal{O}(D/U_\infty)$). Hence, the fact that $St_D = 1$ is optimum in terms of effectiveness of bluff-body separation control indicates that the time scale for actuation must approximately match that characterizing the separated flow region. It is interesting to note that Huang et al. [13,14] found unsteady actuation at $St = 1$ optimum for separation control on a low-pressure turbine blade. As was the case here, the characteristic length scale on which the excitation Strouhal number is based is the length of the separated flow region. In addition to unsteady actuation frequency, the effect of duty cycle was examined. It was found that the effect of duty cycle is small unless it is reduced to a value near 10%, in which case a reduction in flow-control efficiency resulted. Obviously it is desirable to operate the actuators with as small a duty cycle as possible without compromising the ability to control the flow. In this sense, 25% duty cycle was deemed near optimum.

2. Hot-Wire Measurements

To investigate the effect of the plasma actuators on the unsteady vortex shedding characteristics, constant temperature hot-wire anemometry was used to acquire fluctuating streamwise velocity component time-series data. These data were acquired at a sample frequency of 5 kHz, with an anti-alias filter cutoff of 1 kHz. Standard fast Fourier transform (FFT) techniques were used to compute the corresponding autospectral density functions. A blocksize of 8192 points was used for the FFT, and autospectra were ensemble averaged over 128 blocks (a number sufficient to provide smooth, fully converged spectral estimates). The autospectral measurements were made at several representative positions in the near wake. An example of the results obtained is shown in Fig. 10, which presents a comparison of velocity autospectra obtained at $x/D = 4$, $y/D = 1$ for plasma off, steady plasma, and both symmetric and asymmetric unsteady plasma actuation at $f = 50$ Hz, 25% duty cycle conditions. As shown in Fig. 10, velocity autospectra obtained with the plasma off are broadband in nature except for a dominant spectral peak centered at a Strouhal number $St_D = 0.21$, which is associated with

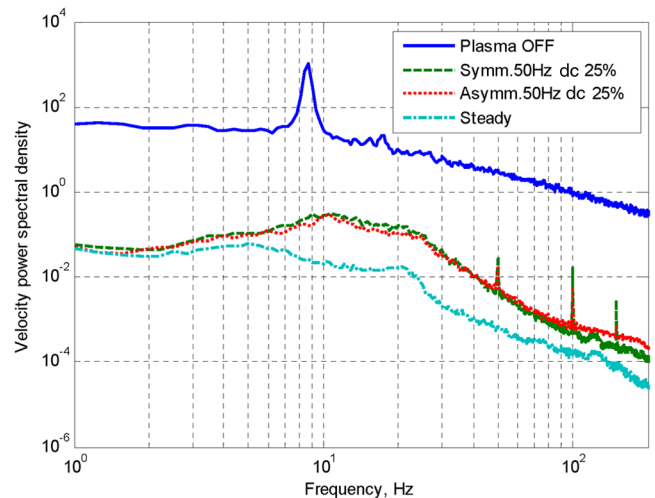


Fig. 10 Comparison of streamwise velocity autospectra for plasma off, steady plasma, and symmetric and asymmetric unsteady plasma actuation conditions.

Karman vortex shedding from the separated flow region. When the four SDBD actuators are operated in steady mode, not only is the discrete peak at $St_D = 0.21$ eliminated, but the broadband spectral levels are greatly suppressed as well. This elimination of Karman shedding and wake turbulence level seems consistent with the flow visualization images shown in Fig. 7. With the unsteady, symmetric, and asymmetric plasma actuation at $f = 50$ Hz, the shedding is also completely suppressed as evidenced by the broadband autospectra shown for those cases in Fig. 10. There is a small discrete peak at $f = 50$ Hz and its harmonics associated with the unsteady plasma-actuation frequency. Note that unsteady plasma actuation also gives rise to a significant reduction in broadband spectral content, which indicates that turbulence levels in the wake have been reduced.

Mean velocity and streamwise-component turbulence intensity cross-stream profiles were obtained at selected x/D locations to characterize the cylinder wake under natural and plasma-actuated conditions. Figures 11 and 12 present sample mean velocity and turbulence intensity profiles, respectively, obtained over a representative range of x/D . In each case, profiles are shown for plasma off, steady plasma, and symmetric unsteady plasma actuation at $f = 50$ Hz ($St_D = 1$), 25% duty cycle. Results for asymmetric unsteady actuation were quite similar to those for the symmetric case and are not presented. From Fig. 11, it is apparent that the wake defect is greatly reduced for the steady plasma case. Unsteady plasma actuation at 25% duty cycle gives rise to a wake defect reduction intermediate between the steady and plasma-off cases. At a given streamwise location, unsteady actuation clearly results in a thinner wake than without the plasma. Note that the effect of the plasma actuation on the wake mean velocity profiles persists with x/D . In effect, the plasma has provided a virtual streamlining of the cylinder.

The plasma-off turbulence intensity profiles exhibit a characteristic saddle shape, and peak intensity occurs in the two wake shear layers. The steady plasma actuation case exhibits the most significant reduction in turbulence levels, and peak intensity occurs on the wake

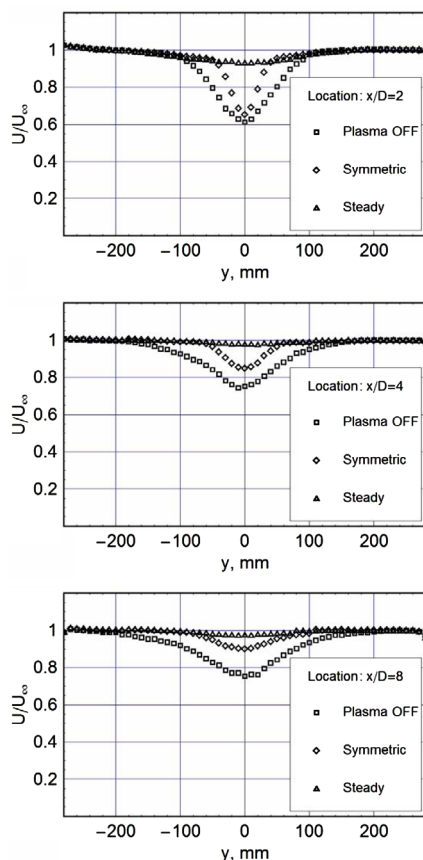


Fig. 11 Comparison of streamwise-component mean velocity profiles in the near wake.

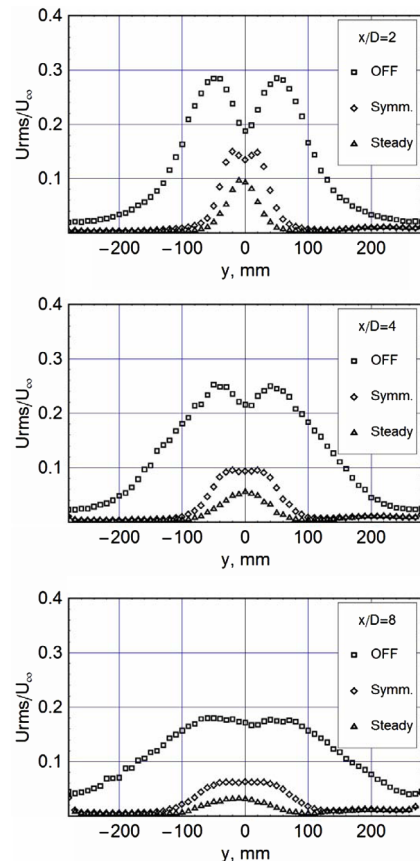


Fig. 12 Comparison of streamwise-component turbulence intensity profiles in the near wake.

centerline. For example, at $x/D = 8$, the peak turbulence intensity under steady plasma actuation is only about 20% of the peak value observed in the natural wake. Unsteady symmetric actuation also gives rise to a significant reduction in wake turbulence levels that is intermediate between the steady plasma and natural wake cases. The turbulence intensity profiles shown in Fig. 12 also serve to demonstrate that the wake is much thinner under steady and unsteady plasma actuation than in the plasma-off case.

3. Near-Wake Particle Image Velocimetry Measurements

The flow visualization and hot-wire measurements presented previously indicate that both steady and unsteady SDBD plasma actuation has a profound effect on the structure of the cylinder wake flowfield. At a given x/D location, not only is the Karman vortex shedding suppressed, but so too is the wake turbulence level. Consequently, the mean velocity defect and wake width are both reduced.

To investigate the physics of this observed modification in wake flow structure, the cylinder near wake was investigated non-intrusively by using PIV measurements. The air upstream of the wind-tunnel inlet was seeded with olive oil droplets of nominally $1 \mu\text{m}$ in diameter that are produced by a TSI atomizer. A model Y120-15 New Wave Research Nd:Yag laser produced double pulses with a $50 \mu\text{sec}$ time interval. The maximum pulse repetition rate for this laser was 15 Hz. PIV images were captured by a PIV CAM 10-30 digital camera. TSI Insight 5 software was used to obtain a vector velocity field from each image pair. Three types of plasma actuation were investigated: steady, unsteady symmetric, and unsteady asymmetric. The unsteady actuation frequency was 50 Hz ($St_D = 1$) with 25% duty cycle. The charge on the droplets resulting from their (shear-dominated) formation process is, at most, only a few hundred electrons. Dimensional reasoning shows that even for the maximum electric field encountered in the experiment, the aerodynamic force

on the droplets is several orders of magnitude larger than the electrostatic force. This result is consistent with the PIV measurements to be presented, which show no evidence of seed particles following electric field lines.

For the unsteady actuation cases, the PIV images were acquired phase locked to the plasma excitation. To do this, the PIV laser was synchronized with the unsteady plasma-actuation circuit. Because the maximum laser pulse repetition rate was smaller than the unsteady actuation frequency, the laser fired every fourth cycle (i.e., PIV images were taken at frequency of 12.5 Hz). The two-component PIV velocity fields were acquired at eight different phase angles (i.e., every 45 deg) with respect to plasma initiation. Conditional sampling was used to acquire 150 image pairs at the same phase of unsteady actuation to form a conditionally averaged flowfield from which animations of the dynamic behavior of the near wake during an actuation cycle were created. To provide sufficient spatial resolution, the camera was positioned to acquire phase-locked flowfield images of several regions in the near wake, and a composite mosaic for a given phase angle was subsequently created.

The conditionally averaged flowfield images (for a given phase angle) were used to compute the spanwise component vorticity field. Figure 13 presents a sequence of images of the phase-averaged spanwise vorticity for unsteady symmetric plasma actuation at $St_D = 1$, 25% duty cycle. In this figure only the phase angles of 0, 90, 180, and 270 deg relative to plasma initiation are presented. When the actuators are on, the region of plasma formation on the cylinder surface is indicated schematically in the figure. Figure 13 shows that

compact, discrete vortices of opposite sign form symmetrically on either side of the wake centerline and emerge from the cylinder surface near the actuators located on the back side of the cylinder. The discrete vortices are shed at the unsteady plasma-actuation frequency of $St_D = 1$. It is important to point out that these are not Bloor–Gerrard type vortices, which are associated with the convective instability of the separated shear layer and would occur at a much higher frequency. The vortices shown in Fig. 13 propagate along the edge of the separated flow region and converge toward the centerline of the near wake. There, the vortices of opposite sign meet, and there appears to be significant cancellation of phase-coherent vorticity of opposite sign. As a result, the spanwise vorticity emanating from the near wake is quite small and phase incoherent in comparison to the natural wake flow. Note also that there appears to be little cross-stream mixing of vorticity of opposite sign.

Figure 14 presents the phase-locked, two-component near-wake velocity field at the same phase angles corresponding to the spanwise vorticity field shown previously in Fig. 13. This figure clearly shows that the region of maximum velocity defect takes on a symmetric, tapered appearance due to the unsteady plasma actuation. Note that the spanwise vortices shown previously in Fig. 13 propagate along the shear layers that form the boundary of the separated flow region. In Fig. 14, these vortices are manifest as wavelike undulations traveling along the outer boundary of the maximum velocity defect region.

The mean velocity magnitude and corresponding mean spanwise vorticity field for steady, symmetric operation of all four actuators is

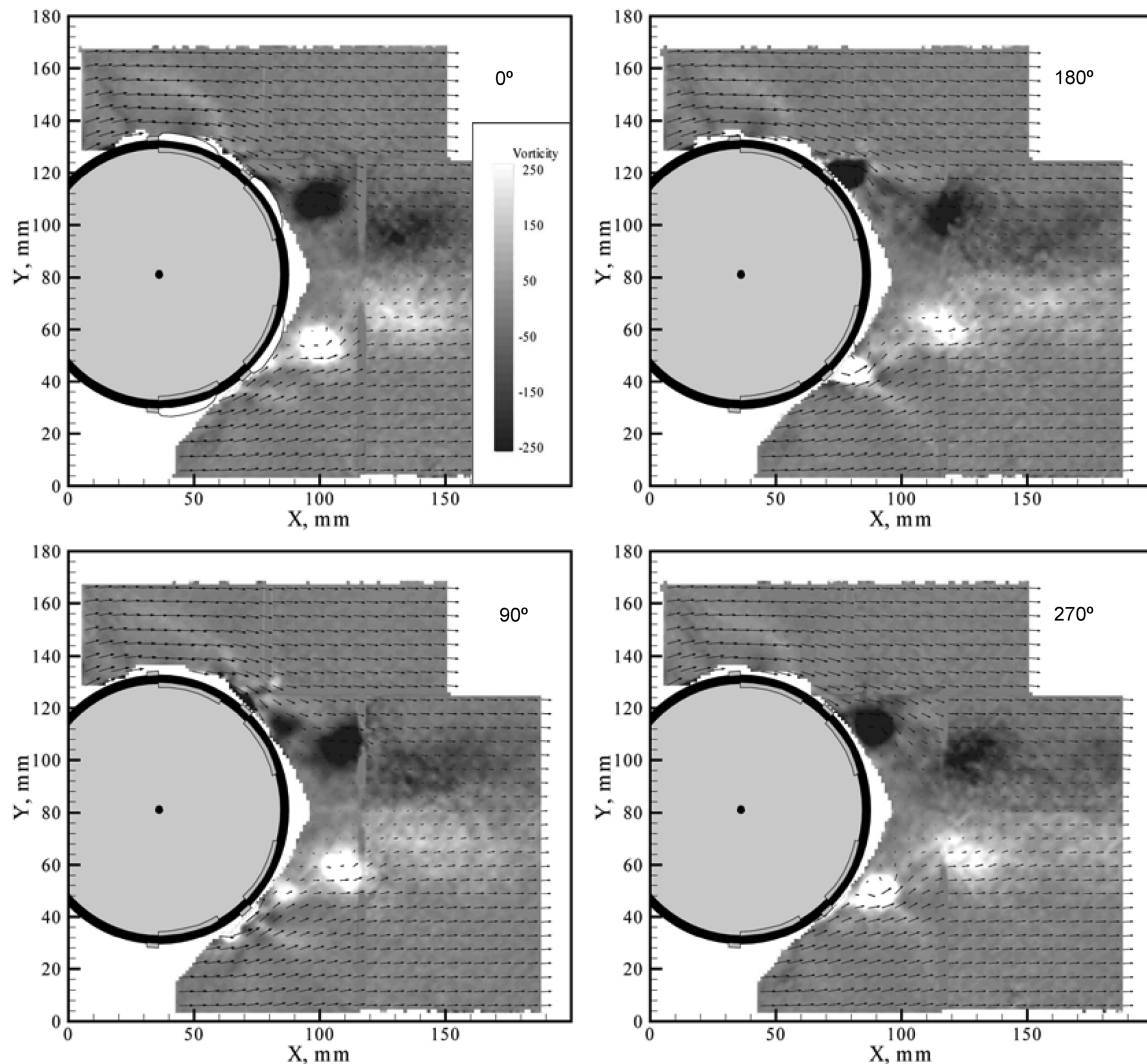


Fig. 13 Near-wake spanwise vorticity field (s^{-1}) phase locked to symmetric plasma actuation ($St_D = 1$, 25% duty cycle). The phase angle is indicated in each case.

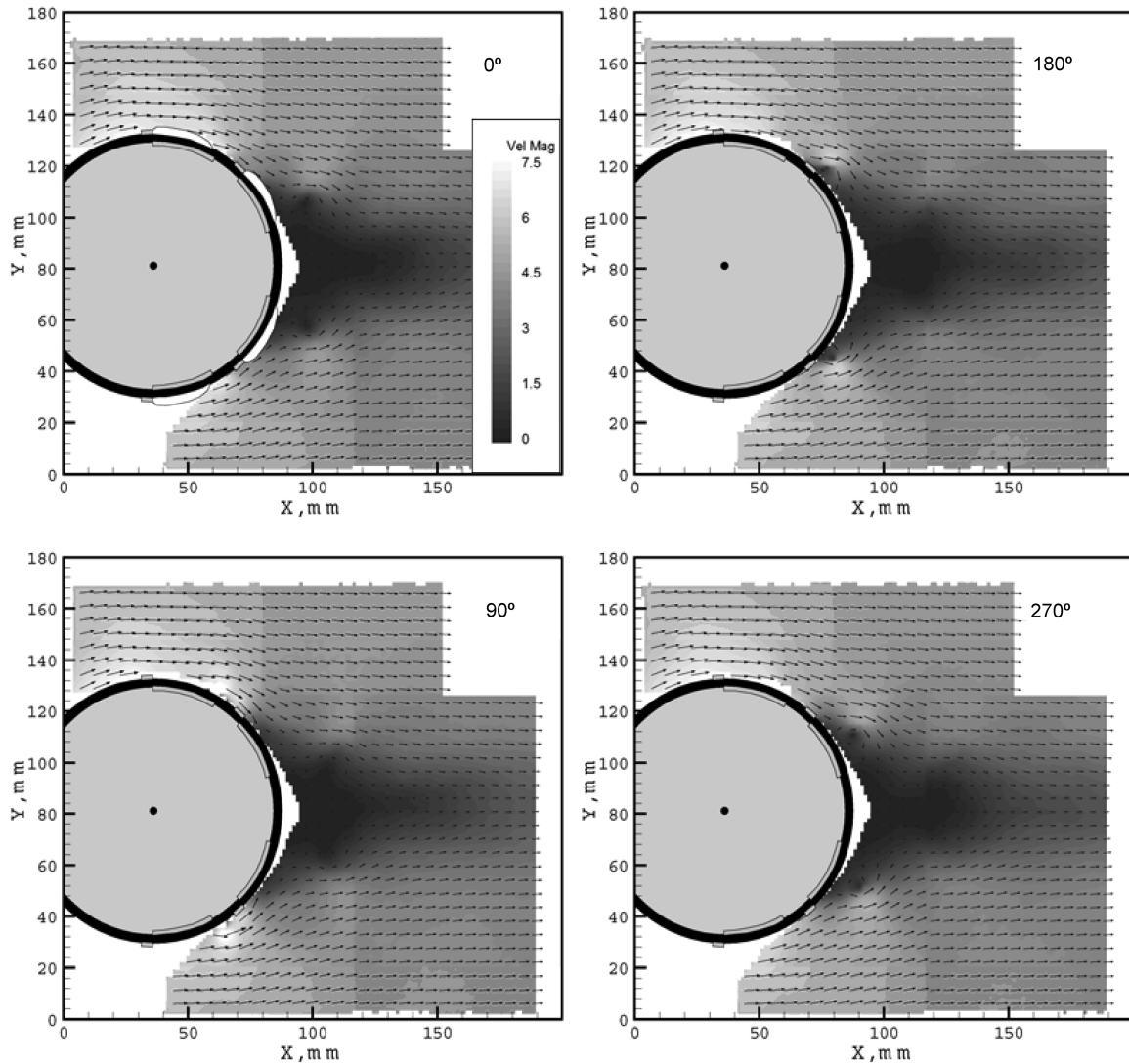


Fig. 14 Near-wake, two-component velocity field (m/s) phase locked to symmetric plasma actuation ($St_D = 1$, 25% duty cycle).

presented in Fig. 15. Because there is no phase reference for steady plasma actuation, these figures present ensemble-averaged fields. The velocity field shows that, with steady plasma-induced blowing, the flow remains attached to the cylinder surface, and the separated

flow region is very small. This is consistent with earlier results of Thomas et al. [12], who demonstrated greater than 90% drag reduction using steady blowing with two actuators on a cylinder in crossflow for $Re_D = 1.2 \times 10^4$. The vorticity field of Fig. 15 shows

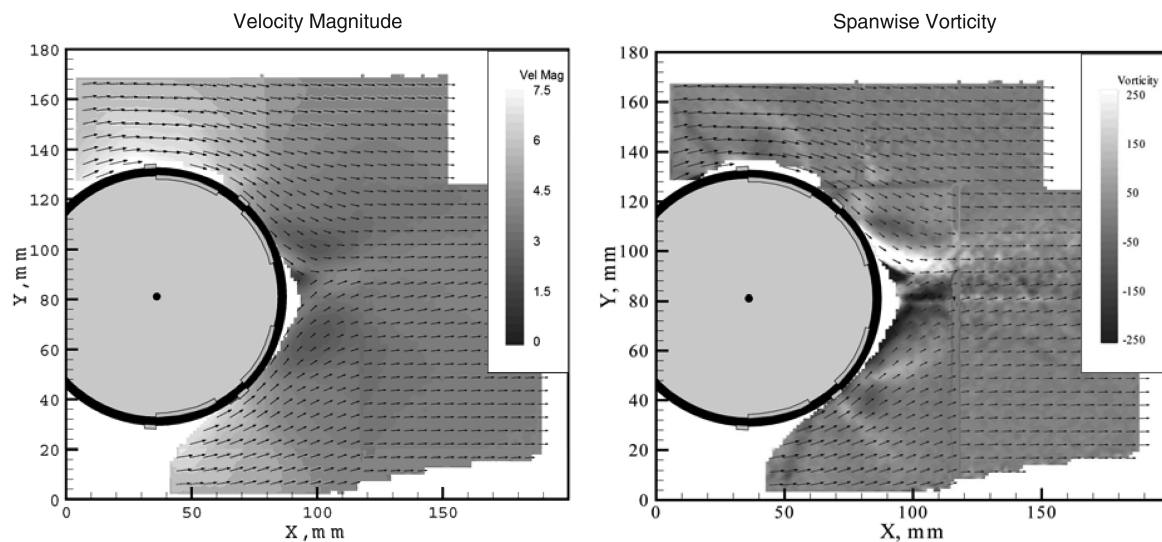


Fig. 15 Near-wake, ensemble-averaged velocity magnitude (m/s) and spanwise vorticity (s^{-1}) fields for steady, symmetric plasma actuation.

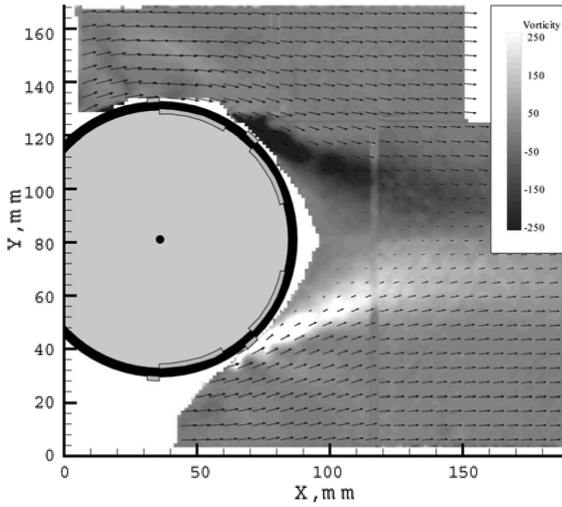


Fig. 16 Ensemble-averaged spanwise vorticity (sec^{-1}) for unsteady, symmetric plasma actuation.

that two shear layers containing vorticity of opposite sign bound the separated region and meet on the wake centerline. The downstream cylinder wake contains little coherent spanwise vorticity.

To provide a more direct comparison of the effects of steady and unsteady symmetric plasma actuation on the near wake, Fig. 16 presents the ensemble-averaged spanwise vorticity field for unsteady

actuation at $St_D = 1$, 25% duty cycle. Comparison with the ensemble-averaged spanwise vorticity shown in Fig. 15 for steady blowing highlights both the smaller separated region (associated with delayed separation) for the steady actuation case as well as a more rapid demise of spanwise vorticity.

In a first attempt to investigate the effect of plasma-actuator phasing, the actuators were operated in an asymmetric mode. As in the unsteady, symmetric case, the excitation Strouhal number remained set to $St_D = 1$, and the duty cycle was 25%. In this case, however, the top and bottom pairs of actuators were fired in antiphase as shown in Fig. 4. Figure 17 presents phase-locked spanwise vorticity for selected phase angles relative to the firing of the top pair of actuators. The results are remarkably similar to those shown previously in Fig. 13, with the exception that the shed vortices are now arranged asymmetrically with respect to the wake centerline. As before, the vortex shedding occurs at the plasma unsteady-actuation region. As in the symmetric forcing case, the separated flow region is quite small, and the apparent elimination of large-scale spanwise vorticity downstream of the cylinder still occurs. In this manner, both symmetric and asymmetric unsteady actuation are observed to eliminate Karman shedding and reduce wake turbulence levels as demonstrated in the autospectra of Fig. 10.

4. Near-Field Microphone Measurements

In this section, measurements are presented that document the effect of the plasma actuation on the near-field pressure fluctuations measured with a microphone that is flush mounted in the wind-tunnel wall. The transducer used in this experiment was a 1/2 in. ACO

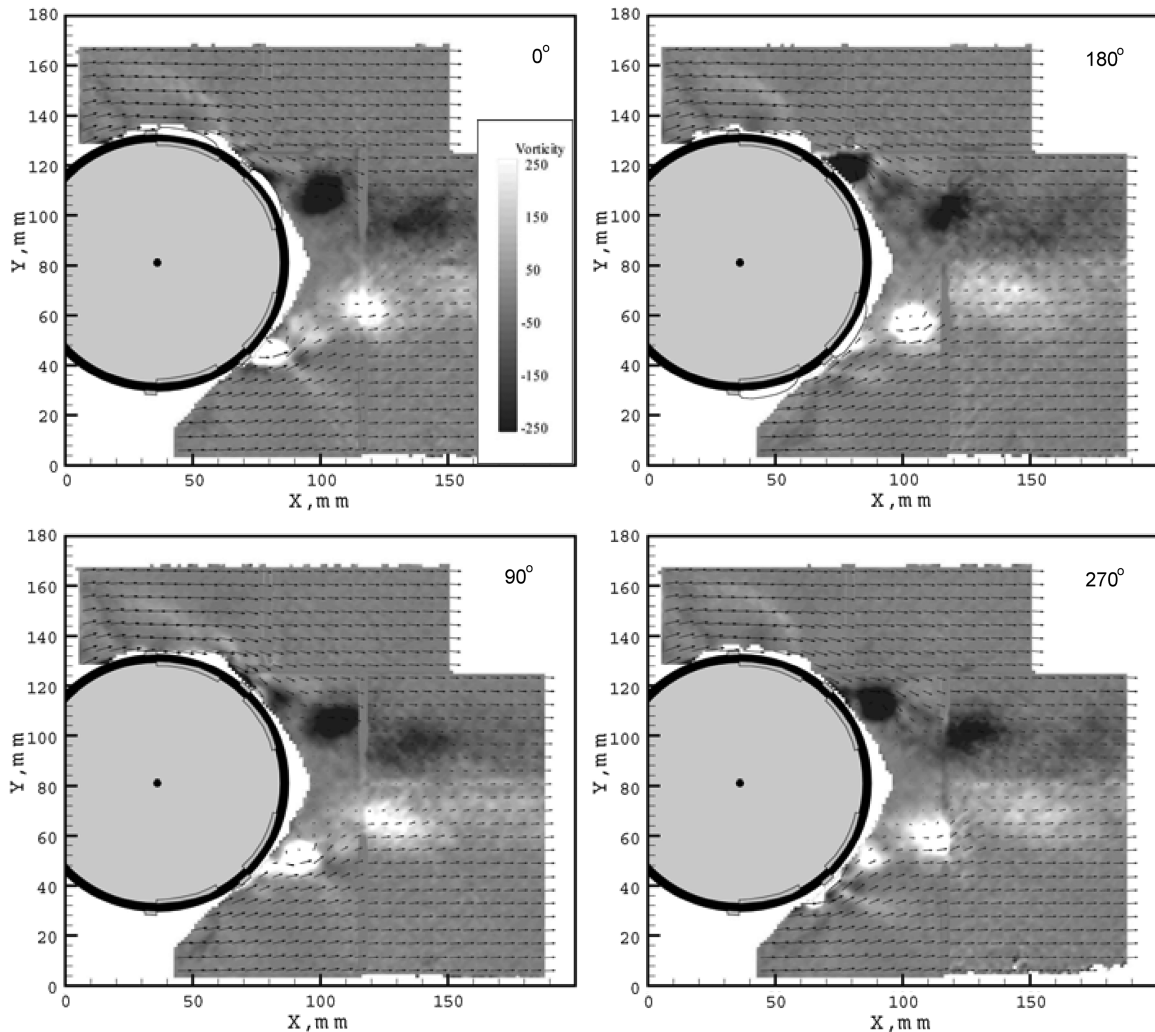


Fig. 17 Near-wake spanwise vorticity field (sec^{-1}) phase locked to asymmetric plasma actuation ($St_D = 1$).

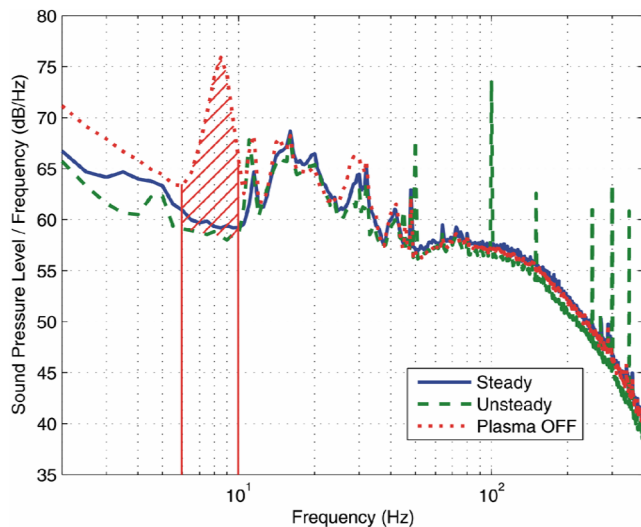


Fig. 18 Effect of plasma actuation on near-field SPL spectra.

model 7046 free-field condenser microphone with 51.3 mV/Pa output sensitivity. The microphone was preamplified with an ACO 1/2 in. XLR model 412 preamp powered by a two-channel 200/28V dc PS2900 power supply. The microphone signal was acquired by a personal computer using a Microstar iDSC1816 A/D board. This board has onboard software-controlled anti-aliasing filters. The microphone was flush mounted to the bottom wall of the wind-tunnel test section and was located 150 mm ($\Delta x/D = 1.5$) downstream of the cylinder. The data were acquired at a sample frequency of 1024 Hz, with an anti-alias filter cutoff of 400 Hz. The power spectral density (PSD) of the signal was calculated with a frequency resolution of 0.5 Hz. Smooth, fully converged spectral estimates were obtained by ensemble averaging 256 blocks of 2048 sample points each.

The fluctuating pressure measured at the microphone will contain contributions from the cylinder wake, the tunnel wall boundary layer, and downstream fan noise. For this reason, the objective of the microphone measurements reported in this paper is to document *changes* in the acoustic spectrum that result from operation of the actuators in steady and unsteady mode. Sample power spectral density plots of the fluctuating pressure are presented in Fig. 18. These were obtained at $Re_D = 3.3 \times 10^4$. Three cases are shown: 1) no actuation, 2) steady actuation, and 3) unsteady, symmetric actuation at 50 Hz with a 25% duty cycle. Near-field pressure fluctuations at the Karman vortex shedding frequency are apparent in the no-actuation spectrum (i.e., “plasma-off” case). Note that this spectral peak is completely suppressed in both the steady and unsteady plasma-actuated cases. The power spectral density was numerically integrated from 6 to 10 Hz to obtain a sound pressure level associated with the Karman wake vortices. Calculations show that the near-field sound pressure level was reduced by plasma actuation by 13.3 ± 0.1 dB. This corresponds to a reduction in mean-square fluctuating pressure by a factor of about 21.4. The difference between steady and unsteady actuated spectra is small except for the presence of a 50-Hz unsteady actuation frequency tone and its harmonics. The contribution from the discrete peaks associated with unsteady plasma actuation was evaluated similarly and found to be small in comparison to the level associated with the Karman wake vortices. After accounting for the discrete spectral peaks, there remained a net reduction in sound pressure level (SPL) of 4 ± 0.1 dB.

V. Conclusions

The results of the flow-control experiments presented in this paper clearly demonstrate the feasibility of the plasma-fairing concept for effectively streamlining bluff-body flows. In particular, it is

demonstrated that a (sparse) array of surface-mounted SDBD plasma actuators can effectively streamline a circular cylinder in crossflow. Steady operation of the actuators is shown to drastically reduce the degree of flow separation and the associated Karman vortex shedding is eliminated. As a consequence, both the wake mean velocity defect and width are reduced as shown in the mean velocity profiles in Fig. 11. An associated benefit of the steady plasma actuation is that peak turbulence levels in the downstream wake are reduced by approximately 80% from those in the natural wake.

It is shown that the use of unsteady plasma actuation at 25% duty cycle and a frequency corresponding to $St_D = 1$ also eliminates Karman shedding, and downstream wake turbulence levels are reduced. Both symmetric and asymmetric unsteady actuation are shown to produce similar effects. For unsteady actuation, compact vortices are shed at the unsteady plasma-actuation frequency and propagate to the wake centerline, where considerable cancellation of coherent vorticity of opposite sign occurs. In this case, the peak turbulence level in the wake is reduced by 66% relative to peak values in the natural wake. Further, this is accomplished with only 25% of the power input to the actuators required for steady actuation. However, lower duty cycles approaching 10% were found to lead to reduced flow-control effectiveness.

Microphone measurements confirm the reduction of near-field pressure fluctuations associated with suppression of vortex shedding. For both steady and unsteady actuation, near-field sound pressure levels are reduced by 13.3 dB in a frequency band centered on the shedding frequency. Because unsteady plasma actuation is associated with an unsteady body force, it produces tones at the actuation frequency and its harmonics. In the experiments reported here, there is still a net SPL reduction of 4 dB despite the tones. However, for those flow-control applications focused on aerodynamic noise reduction, there is an advantage in using the plasma in a steady mode of operation.

If C_μ is computed based upon integration of measured plasma-induced wall-normal mean velocity profiles obtained 45 deg downstream of the actuator (with no external flow), values of 0.011 and 0.003 are obtained for steady and unsteady actuation, respectively. The values of the momentum coefficient quoted previously must be viewed with caution, however, because this parameter does not account for the shape of the actuator-induced velocity $V_j(y)$ nor its thickness with respect to the viscous wall layer. Clearly, these must be important parameters in separation control applications. Further, it can be demonstrated that in the case of unsteady actuation, the time average plasma-induced velocity profile obtained under the no-flow condition will not be the same as with external flow. This is a consequence of the fact that the effect of the actuator is to promote cross-stream mixing through the creation of large-scale vortices at the unsteady actuation frequency.

With fixed actuator authority, the effectiveness of the flow control will obviously be gradually lost as the Reynolds number is increased [12]. For a commercial transport on landing approach, the Reynolds number for the flow over the landing gear oleo will be $\mathcal{O}(10^6)$. Hence, for application in flight, the actuation authority must undergo a commensurate increase. Increased body force can be achieved by 1) increasing the applied voltage and optimizing the waveform, 2) using improved dielectric materials for construction of the actuators, and 3) increasing the number of actuators in series. The behavior of multiple actuators in series has been examined by Post [11] and Forte et al. [19]. It has been demonstrated that the thrust due to actuators in series is additive. The utility of adding additional actuators is clear by comparing the results of this paper, which uses four actuators on the cylinder surface, with those of Thomas et al. [12], which used only two. The Reynolds number range for effective flow control more than doubled with the addition of two actuators.

In addition to overcoming problems associated with achieving sufficient actuator authority, the extreme geometric complexity of landing gear must be addressed. It has been shown that the removal of small parts like hoses, tubes, etc. reduces high-frequency gear noise [1,20]. Hence, it is envisioned that landing gear noise control might be best achieved by shielding small elements behind larger elements, which are effectively streamlined through a combination of passive

shaping and plasma actuation. In such a case, the plasma actuation could be used for wake vectoring away from downstream gear elements and/or suppression of shedding and fine-scale turbulence.

Acknowledgments

This work is supported by NASA Langley Research Center under NAG1-03076 monitored by David Lockard and Bart Singer. The authors gratefully acknowledge this support.

References

- [1] Michel, U., Barsikow, B., Helbig, J., Hellmig, M., and Schuttpelz, M., "Flyover Noise Measurements on Landing Aircraft with a Microphone Array," AIAA Paper 1998-2336, 1998.
- [2] Lazos, B., "Surface Topology on the Wheels of a Generic Four-Wheel Landing Gear," *AIAA Journal*, Vol. 40, No. 12, 2002, pp. 2402–2411.
- [3] Li, F., Khorrami, M. R., and Malik, M. R., "Unsteady Simulation of a Landing-Gear Flow Field," AIAA Paper 2002-2411, 2002.
- [4] Lockard, D. P., Khorrami, M. R., and Li, F., "Aeroacoustic Analysis of a Simplified Landing Gear," AIAA Paper 2003-3111, 2003.
- [5] Ffowcs Williams, J. E., and Hawkins, D. L., "Sound Generation by Turbulence and Surfaces in Arbitrary Motion," *Philosophical Transactions of the Royal Society of London, Series A: Mathematical and Physical Sciences*, Vol. 264, No. 1151, 1969, pp. 321–342. doi:10.1098/rsta.1969.0031
- [6] Fridman, A., and Kennedy, L. A., *Plasma Physics and Engineering*, Taylor and Francis, New York, 2004.
- [7] Enloe, C. L., McLaughlin, T. E., VanDyken, R. D., Kachner, K. D., Jumper, E. J., Corke, T. C., Post, M., and Haddad, O., "Mechanisms and Responses of a Single Dielectric Barrier Plasma Actuator: Geometric Effects," *AIAA Journal*, Vol. 42, No. 3, 2004, pp. 595–604. doi:10.2514/1.3884
- [8] Enloe, C. L., McLaughlin, T. E., VanDyken, R. D., Kachner, K. D., Jumper, E. J., Corke, "Mechanisms and Responses of a Single Dielectric Barrier Plasma Actuator: Plasma Morphology," *AIAA Journal*, Vol. 42, No. 3, 2004, pp. 589–594. doi:10.2514/1.2305
- [9] Gibalov, V. I., and Pietsch, G. J., "The Development of Dielectric Barrier Discharges in Gas Gaps and on Surfaces," *Journal of Physics D: Applied Physics* Vol. 33, 2000, pp. 2618–2636. doi:10.1088/0022-3727/33/20/315
- [10] Raizer, Yu. P., *Gas Discharge Physics*, Springer-Verlag, Berlin, 1991.
- [11] Post, M. L., "Phased Plasma Actuators for Unsteady Flow Control," Master's Thesis, University of Notre Dame, Notre Dame, IN, 2001.
- [12] Thomas, F. O., Kozlov, A., Corke, T. C., "Plasma Actuators for Landing Gear Noise Control," AIAA Paper 2005-3010, 2005.
- [13] Huang, J., Corke, T. C., and Thomas, F. O., "Plasma Actuators for Separation Control of Low-Pressure Turbine Blades," *AIAA Journal*, Vol. 44, No. 1, pp. 51–57. doi:10.2514/1.2903, 2006.
- [14] Huang, J., Corke, T. C., and Thomas, F. O., "Unsteady Plasma Actuators for Separation Control of Low-Pressure Turbine Blades," *AIAA Journal*, Vol. 44, No. 7, 2006, pp. 1477–1487. doi:10.2514/1.19243
- [15] Mueller, T. J., "On the Historical Development of Apparatus and Techniques for Smoke Visualization of Subsonic and Supersonic Flow," AIAA Paper 80-0420-CP, 1980.
- [16] Bloor, M. S., "The Transition to Turbulence in the Wake of a Circular Cylinder," *Journal of Fluid Mechanics*, Vol. 19, No. 2, 1964, pp. 290–304. doi:10.1017/S0022112064000726
- [17] Gerrard, J. H., "A Disturbance Sensitive Reynolds Number Range of the Flow past a Circular Cylinder," *Journal of Fluid Mechanics* Vol. 22, No. 1, 1965, pp. 187–196. doi:10.1017/S0022112065000666
- [18] Williamson, C. H. K., "Advances in our Understanding of Vortex Dynamics in Bluff Body Wakes," *Journal of Wind Engineering and Industrial Aerodynamics*, Vol. 69, No. 71, 1997, pp. 3–32. doi:10.1016/S0167-6105(97)00145-1
- [19] Forte, M., Jolibois, J., Moreau, E., Touchard, G., Cazalens, M., "Optimization of a Dielectric Barrier Discharge Actuator by Stationary and Non-Stationary Measurements of the Induced Flow Velocity: Application to Airflow Control," AIAA Paper 2006-2863, 2006.
- [20] Rackl, R. G., Miller, G., Guo, Y., Yamamoto, K., "Airframe Noise Studies: Review and Future Direction," NASA CR 2005-213767, 2005.

A. Tumin
Associate Editor